A Comparative Performance Analysis of GPS L1 C/A, L5 Acquisition and Tracking Stages under Polar and Equatorial Scintillations

A Comparative Performance Analysis of GPS L1 C/A, L5 Acquisition and Tracking Stages Under Polar and Equatorial Scintillations

CANER SAVAS
Politecnico di Torino, Turin, Italy

GIANLUCA FALCO
LINKS Foundation, Turin, Italy

FABIO DOVIS
Politecnico di Torino, Turin, Italy

This article provides a comparative performance analysis of different acquisition and tracking methods of GPS L1 C/A and GPS L5 signals testing their robustness to the presence of scintillations in the propagation environment. This article compares the different acquisition methods in terms of probabilities of detection/false alarm, peak-to-noise floor ratios for the acquired signal and execution time, assessing the performance loss in the presence of scintillations. Moreover, robust tracking architectures that are optimized to operate in a harsh ionospheric environment have been employed. The performance of the carrier tracking methods, namely, traditional phase-locked loop (PLL) and Kalman filter based-PLL, have been compared in terms of the standard deviation of Doppler estimation, phase error, phase lock indicator (PLI), and phase jitter. The article is based on real global navigation satellite systems (GNSS) signals affected by significant phase and amplitude scintillation effects, collected at the South African Antarctic research base (SANAE IV) and Brazilian Centro de Radioastronomia e Astrofisica Mackenzie (CRAAM) monitoring stations. Performance is assessed exploiting a fully software GNSS receiver, which implements the different architectures. The comparative analysis allows to choose the best setting of the acquisition and tracking parameters, in order to allow the operation of signal acquisition and tracking at a required performance level under scintillation conditions.

Manuscript received January 16, 2019; revised June 1, 2019, October 4, 2019, April 30, 2020, and June 22, 2020; released for publication July 16, 2020. Date of publication July 27, 2020; date of current version February 9, 2021.

DOI. No. 10.1109/TAES.2020.3011999

Refereeing of this contribution was handled by O. Osechas.

This work was supported by European Union's Horizon 2020 Research and Innovation Programme through the TREASURE project under the Marie Skodowska-Curie Actions under Grant 722023.

Authors' addresses: Caner Savas and Fabio Dovis are with the Department of Electronics and Telecommunications, Politecnico di Torino, 10129 Turin, Italy, E-mail: (caner.savas@polito.it; fabio.dovis@polito.it); Gianluca Falco is with the LINKS Foundation, 10138 Turin, Italy, E-mail: (gianluca.falco@linksfoundation.com). *(Corresponding author: Caner Savas.)*

I. INTRODUCTION

The third civilian global positioning system (GPS) signal L5 is being broadcast by 12 Block-IIF GPS satellites [1]. The L5 signal, as a new signal with advanced features, represents an opportunity of enhanced performance for the global navigation satellite systems (GNSS) receivers. Having a data-free channel, which uses longer codes at higher chipping rates, and having the chance to receive at an higher power than L1 C/A provide an appealing improvement in acquisition/tracking process of GNSS receivers [2]. Moreover, in combination with L1 C/A, it also allows users to have frequency diversity for the correction of the ionospheric error and to monitor the ionospheric irregularities.

The new L5 signal, as well as any GNSS signal, undergoes severe propagation effects such as phase shifts, group delays, and amplitude variations while propagating through the ionosphere [3]. Ionospheric irregularities affect the GNSS signals in two ways, namely, refraction and diffraction, and both of them are caused by the group delay and phase advance of GNSS signals [4]. Both the aforementioned effects that are usually denoted as scintillation effects cause fluctuations in the signal amplitude and phase of the received signals. Large-scale variations in both signal power and phase with the increased measurement noise level severely degrade the GNSS receiver performance by preventing the receiver from correctly acquiring the GNSS signals or causing loss-of-lock when the signals are tracked.

The aim of this article is to present a comparative study of different acquisition and tracking methods for GPS L5 and L1 C/A signals in order to test their robustness to the presence of phase and amplitude scintillations in the propagation environment. In order to evaluate the effects of such scintillations on a GNSS receiver, we first focused our analysis on the acquisition part, which is used to find the visible satellites and to obtain the rough estimates of the code phase and Doppler shift. In the literature, in principle, there are three main classes of acquisition techniques: coherent, noncoherent, and coherent with sign recovery [5]. All these approaches are considered by the methods tested in this article. In order to analyze and compare the performances of different acquisition techniques, as explained in [6], we compare different metrics: the probabilities of detection/false alarm, the peak-to-noise floor ratios for the acquired signals, and the execution time of the signal acquisition. Preliminary results on the acquisition in case of strong scintillations were presented in a recent paper [7]. Having analyzed the scintillation effect on the acquisition part, we focused on another key design component of a GNSS receiver, namely, the carrier-tracking part. By employing phase-locked loop (PLL) and Kalman filter (KF) based carrier-tracking algorithms for GPS L1 C/A and L5

signals, we aim at mitigating the scintillation effect by considering robust architectures optimized to operate in a harsh ionospheric environment. In order to evaluate and compare the performances of different architectures, the residual effects on the receiver observables and internal parameters have been used.

Even if the aforementioned acquisition and tracking structures are well known in the literature, the scope of this article is to select the optimal acquisition and tracking parameters able to make a GPS receiver robust enough to work even under strong scintillation conditions. Deep amplitude fades that can be observed in equatorial scintillation events over a significant duration can prevent the acquisition of the signal within a GNSS receiver, or anyway cause loss of lock or degradation in pseudorange and carrier phase measurements. Phase scintillation also adversely affects the operation of PLL and it leads to cycle slips, navigation bit errors, and complete loss of lock [8].

It can be pointed out that most of the studies in the literature do not consider the effects of scintillation on the acquisition stages of L1 C/A and L5 signals under real, moderate, and strong scintillation events. For example, in [5], the authors provided three different acquisition strategies, but they are analyzed in details only from a statistical point of view, by using Monte Carlo simulations to support their theoretical analysis. Moreover, even if the authors in [9]–[12] propose different L5 acquisition algorithms, the performance evaluation of the methods is limited either on simulation or on real data not affected by scintillation.

Nonetheless, as far as the tracking stage is concerned, in order to be able to cope with the fading and abrupt phase changes of the scintillation effect, some additional robust architectures have been investigated in the recent years. For example, different methods have been proposed to tune the dynamic models by exploiting the knowledge about the scintillation level as in [13] or by using the signal carrier-to-noise (C/N_0) levels as a control parameter to improve the tracking of the incoming signals as in [14] and [15]. However, these types of adaptive algorithms require parallel computation of the scintillation level and to feed back such information to the tracking stage. Moreover, in [16], different constant-bandwidth PLL structures and KF-based tracking are compared under scintillation; unfortunately, the analysis is limited to an equatorial scintillation event in terms of loss-of-lock duration only.

Moreover, in order to show the performance of the proposed signal tracking techniques, different ionospheric scintillation models have been developed. Some of the proposed algorithms are tested by using the Cornell scintillation model as in [17] and [18], others the global ionospheric scintillation model [19], [20] or the wideband model as in [21] and [22]. It can be stressed that most of the aforementioned studies do not consider the effects of scintillation on both L1 C/A and L5 signals under real scintillation events, but they limit the analysis to simulations. The innovative aspect of this article is a detailed performance comparison of both L1 C/A and L5 signals at the acquisition and tracking stages under real phase and amplitude scintillations.

This article is organized as in the following. In Section II, we start with a short summary of the phase and amplitude scintillations and analysis of the real data collected at low and high latitude sites. Section III covers the general characteristics of GPS L5 and GPS L1 C/A signals. In Section IV, four L5 and three L1 C/A acquisition methods are implemented and the detailed performance comparison analysis under both scintillation and clean signals are presented. In Section V, we revise the carrier tracking structures: traditional PLL and KF-based PLL, and provide the comparative analysis with the results of the real data. Eventually Section VI, concludes this article.

II. OVERVIEW OF IONOSPHERIC SCINTILLATION

During a scintillation event, in order to mitigate the effect of the rapid fluctuations in the amplitude and phase of the signal, the solutions could be to minimize the effects of the scintillation by making the signal acquisition/tracking parts more robust within the receiver or using complementary solutions such as signals of different GNSS constellations or other navigation sensors. For this reason, detecting and monitoring the scintillation effects to estimate the scintillation in its early stages and measure the scintillation parameters have gained importance. Although GNSS signals are themselves affected by the ionospheric scintillation too, observation of the received GNSS signals can be a possible option to estimate the ionospheric scintillation [23].

There are two parameters that are typically used to indicate the amount of scintillation effect in a satellite signal and that are computed by employing the tracking outputs [23]: S_4 and σ_ϕ. S_4 index is the standard deviation of the received power as computed from the prompt correlator samples normalized by its mean value:

$$S_4 = \sqrt{\frac{\langle I^2 \rangle_T - \langle I \rangle_T^2}{\langle I \rangle_T^2}} \tag{1}$$

where I is the detrended signal intensity and $\langle \cdot \rangle_T$ is the average operation over a fixed period T. σ_ϕ index is the standard deviation of the detrended carrier phase measurements

$$\sigma_\phi = \sqrt{\langle \varphi^2 \rangle_T - \langle \varphi \rangle_T^2} \tag{2}$$

where φ is the detrended carrier phase measurement. accumulated delta range that corresponds to the accumulation of the estimated phase by the corresponding carrier tracking loop is used for the carrier phase observation.

In phase-detrending algorithms, the phase measurements are passed through three cascaded second-order high-pass filters and all low-frequency effects are removed. In amplitude-detrending algorithms, second-order low-pass filters are used. Useful material in the design of the detrending filters can be found in [23]. As far as the computation of the scintillation level is concerned, it is required to collect data at high rate at the tracking level (e.g., raw data at 50 Hz rate from the tracking outputs are used) and the scintillation parameters are typically computed every 1 min. S_4 index typically varies between 0 and 1, while σ_ϕ index typically stays below 1.0 radian. When there is no scintillation, the

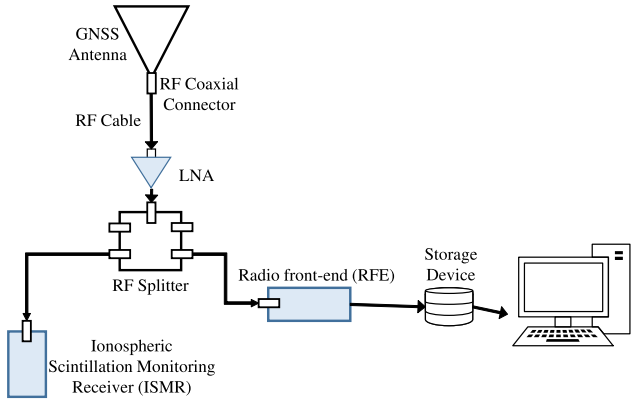

Fig. 1. GNSS raw IF data collection test setup.

indices are below 0.2. For weak scintillation, the indices are normally between 0.2 and 0.5. When S_4 and σ_ϕ values are between 0.5 and 0.7, the event is usually classified as moderate scintillation. If they are higher than 0.7, the events are evaluated as strong scintillation cases.

A. Data Collection

Throughout the presented analyses in this article, we based our investigation on real data affected by phase and amplitude scintillations. Fig. 1 shows the data collection setup.

GNSS signals have been captured by an active antenna of which built-in amplifier has a gain of 39 ± 2 dB gain and maximum 2.8 dB noise figure. The low noise amplifier of the front-end has 30 dB gain and 3 dB noise figure. However, depending on the test setup, due to the antenna cable, coaxial connectors, and one-to-four splitter, additional losses are experienced. An interested reader can find useful material about the design of monitoring stations of this kind in [3].

The radio front-end (RFE) samples the GNSS signal after a downconversion to intermediate frequency (IF), storing the raw samples of the signals. This configuration captures a series of 50-min IF recordings each day. The data-collecting setup is a part of DemoGRAPE project and a custom-design solution based on a multifrequency and multiconstellation GNSS data grabber [24], [25]. RFE sampling frequencies for L1 C/A and L5 signals are 5 and 30 MHz, respectively, and it digitizes them to complex 8-b samples. Raw sampled GNSS IF data are postprocessed in the software receiver. According to the levels of computed S_4 and σ_ϕ parameters from the tracking outputs, scintillation datasets are categorized.

B. Analysis of Scintillation Data

Due to the quasi-random nature of a scintillation event, it is very difficult to model its occurrence, which is determined by several factors such as solar and geomagnetic activity, geographic location, the season of the year, and local time [24]. However, in [26], the authors provided a statistical analysis of intensity, duration and occurrence frequency of amplitude, and phase scintillation by analyzing

TABLE I
Specifications of the Scintillated Data

	Date	Station	Coordinates
1	May 8, 2016 Aug 17, 2016	South African Antarctic Research Base (SANAE-IV), Antarctic	Lat.:71.67278°S Long.: 2.840556°W
2	Sept 13, 2017	Centro de Radioastronomia e Astrofisica Mackenzie (CRAAM), Brazil	Lat: 23.5474825°S Long: 46.6523133°E

the collected datasets in both high latitude and equatorial regions. It shows that scintillation events observed at the equatorial region are typically more severe with deeper and faster signal power fadings and longer durations. Moreover, in [27], the authors assessed a statistical relationship between the location and the scintillation effect, which shows that at high latitudes, phase scintillation occurs more often than amplitude scintillation. Furthermore, in [26], the analysis also shows that while the mean duration of amplitude scintillation events observed in the equatorial region lasts 12.4 min, the mean duration of the phase scintillation events in the polar region is 5.6 min. An interested reader can find more statistics related to scintillation events in [26] and [27].

In the light of these pieces of information, some specific data that include strong, moderate, and weak scintillation events were chosen as representative of different scintillation intensity. The analyzed scintillated data in this article are summarized in Table I.

Fig. 2(a) and (b) shows the computed phase scintillation indices for both L1 C/A and L5 signals for the two datasets collected at the Antarctic station. For comparison, the indices computed by a Septentrio PolaRxS PRO professional receiver are also plotted. Due to the polar location of SANAE-IV, the computed S4 indices are low, and only phase scintillation indices have been plotted. The figures show 20-min length portions of the data affected by the phase scintillation events occurred around 8 P.M. and 4 A.M., respectively. Since the ionospheric scintillation effect on GNSS signals is caused by the scattering due to irregularities in the distribution of electrons encountered along the radio propagation path, it rarely occurs on all visible satellites simultaneously [8]. GPS signals that are broadcasted from two Block-IIF satellites (PRN 3 and PRN 9) that transmit signals both on the L1 and L5 frequencies experience strong scintillation ($\sigma_\phi > 0.7$) in these datasets.

Moreover, we consider another event which is observed in the data collected on September 13, 2017 at the Brazilian monitoring station. Fig. 3 shows computed amplitude and phase scintillation indices for both L1 C/A and L5 signals. The figures refer to the portions of the data affected by the amplitude and phase scintillation events occurred starting from 2.15 A.M. as denoted by the sharp increases in the indices. As it can be seen, GPS L1 C/A and L5 signals that are broadcasted from Block IIF (PRN-10) satellite are experiencing strong ($S_4, \sigma_\phi > 0.7$) and moderate ($0.5 < S_4, \sigma_\phi < 0.7$) amplitude and phase scintillations. Since ionosphere is a dispersive medium, the type of interaction between the signal and the ionosphere is dependent on the frequency of the signal and both amplitude and phase scintillation levels have an inverse relation with the signal

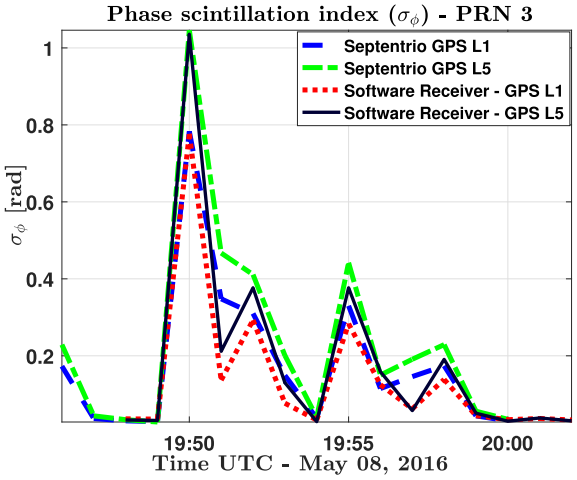

(a)

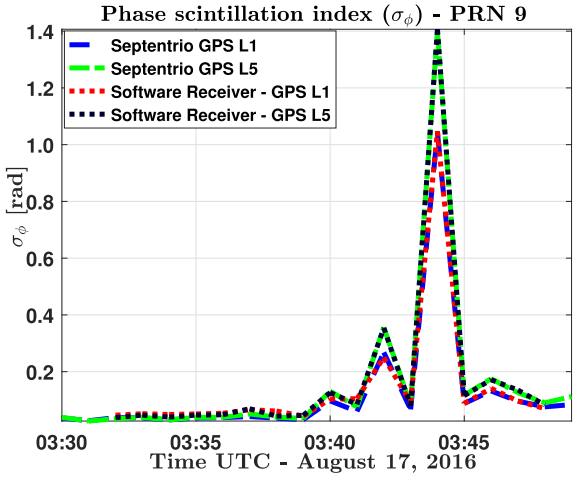

(b)

Fig. 2. Phase scintillation index values at GPS L1 C/A and L5 signals (SANAE IV). (a) Phase Scintillation (PRN3)—May 8, 2016. (b) Phase Scintillation (PRN9)—August 17, 2016.

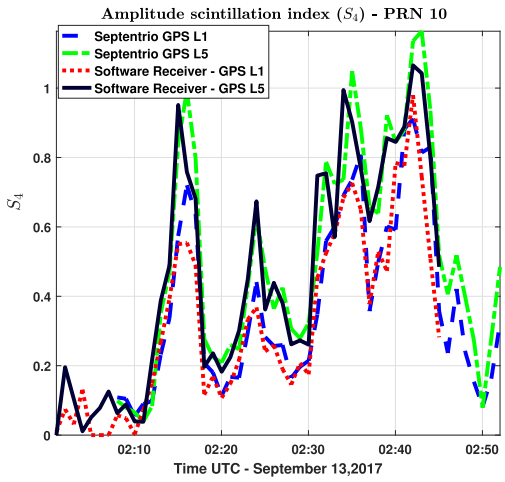

(a)

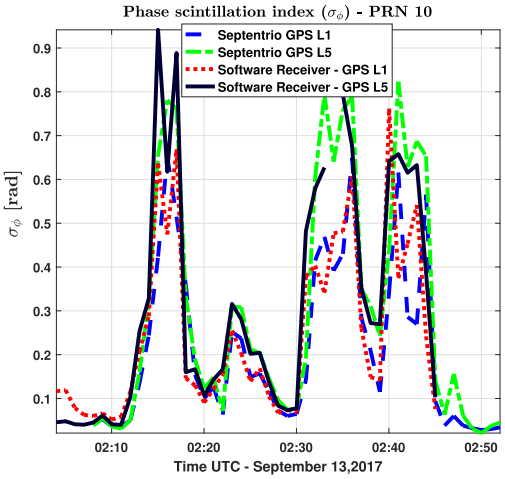

(b)

Fig. 3. Amplitude and phase scintillation index values at GPS L1 C/A and L5 signals—September 13, 2017 (CRAAM). (a) Amplitude scintillation. (b) Phase scintillation.

carrier frequency [8]. Therefore, the L5 signal experiences larger signal fluctuations than the L1 C/A during the 45 min data collection, as expected.

To sum up, S_4 and σ_ϕ parameters reflect the intensity of the scintillation and disturbance rate on the received power and carrier phase measurements [26]. In Sections IV and V, the disturbance effects of these events on the acquisition and the tracking structures will be analyzed.

III. GPS L1 C/A AND L5 SIGNAL STRUCTURES

GPS L1 Coarse/Acquisition (C/A) signal is binary phase-shift keying (BPSK) modulated with the carrier frequency of $f_{L1} = 1575.42$ MHz, while GPS L5 signal is quadrature phase-shift keying (QPSK) modulated and its carrier frequency is $f_{L5} = 1176.45$ MHz. L1 C/A and L5 transmitted signals by a satellite are modeled as follows:

$$s_{L1}(t) = \sqrt{2C_{L1}}c_{L1}(t)d_{L1}(t)\cos(2\pi f_{L1}t) \tag{3}$$

$$s_{L5}(t) = \sqrt{C_{L5}}c_{L5_I}(t)d_{L5}(t)s_{NH_{10}}(t)\cos(2\pi f_{L5}t) + \sqrt{C_{L5}}c_{L5_Q}(t)s_{NH_{20}}(t)\sin(2\pi f_{L5}t) \tag{4}$$

where c_{L1} is the C/A code of 1 ms in length at the chipping rate of 1.023 Mchip/s, d_{L1} is GPS L1 C/A navigation data message at 50 b/s, and d_{L5} is GPS L5 navigation data encoded with forward error correction codes at 100 sample/s. Neuman–Hofman (NH) codes ($s_{\mathrm{NH}_{10}}$ and $s_{\mathrm{NH}_{20}}$) are secondary codes of GPS L5 signal and are 10-b and 20-b long, respectively, with the code rate of 1 kHz. c_{L5_I} and c_{L5_Q} are pseudorandom noise (PRN) codes of in-phase and quadrature channels, which are 1 ms in length with a chipping rate of 10.23 Mchip/s. C_{L1} and C_{L5} correspond to the RF powers of L1 C/A and L5 signals, respectively.

L5 signal includes a navigation data at only in-phase component (i.e., data channel), while quadrature component, namely the pilot channel, carries no message. Furthermore, L5 signal has longer spreading codes for both in-phase and quadrature channels, and higher transmitting power compared to the L1 C/A signal. According to the interface specification document for the block IIF satellites, while the received minimum RF signal strength is −158.5 dBW for the GPS L1 C/A signal, the L5 signal strength is

−154.9 dBW (i.e. −157.9 dBW on each channel, namely, in phase and quadrature) [28]. The results in [29] show that experimentally receiving a mean of 3.5 dB higher power for GPS L5 compared to GPS L1 C/A could be measured. Having a data-free pilot channel, which uses longer codes at higher chipping rates with NH secondary codes, and higher transmitted power than L1 C/A signal, it could have better performance in GNSS receiver. Since the code on L5 is ten times faster than the C/A code, the main peak in the auto-correlation function is sharper by a factor of ten and cross-correlation side lobes are lower than that for the C/A code. Hence, it provides an improvement in the signal tracking capability [2]. Moreover, data-free signal components are useful in low signal-to-noise ratio environments due to the fact that squaring loss caused by the squaring operation, that is used to remove the data modulation, is reduced with the increasing integration time.

After the GNSS signals are received by the antenna, the signals are down-converted and sampled in the RF front-end. Each transmitted satellite signal is separately delayed, attenuated, and affected by Doppler and the sampled signal is the combination of the signals from different visible satellites. Then, the received signal from one satellite can be modeled as follows:

$$\begin{aligned} r_{L1}[n] &= r_{L1}(nT_s) \\ &= \sqrt{2A_{L1}}c_{L1}(nT_s-\tau_{L1,0})d_{L1}(nT_s-\tau_{L1,0}) \\ &\quad\times\cos(2\pi(f_{IF,L1}+f_{L1,0})nT_s-\varphi_{L1,0}) \\ &\quad+\eta_{L1,IF}(nT_s). \end{aligned} \tag{5}$$

$$\begin{aligned} r_{L5}(nT_s) &= \sqrt{A_{L5}}c_{L5_I}(nT_s-\tau_{L5,0})d_{L5}(nT_s-\tau_{L5,0}) \\ &\quad\times s_{NH_{10}}(nT_s-\tau_{L5,0}) \\ &\quad\times\cos(2\pi(f_{IF,L5}+f_{L5,0})nT_s-\varphi_{L5,0}) \\ &\quad+\sqrt{A_{L5}}c_{L5_Q}(nT_s-\tau_{L5,0})s_{NH_{20}}(nT_s-\tau_{L5,0}) \\ &\quad\times\sin(2\pi(f_{IF,L5}+f_{L5,0})nT_s-\varphi_{L5,0}) \\ &\quad+\eta_{L5,IF}(nT_s). \end{aligned} \tag{6}$$

where τ_0, f_0, φ_0 are the code delay, Doppler frequency offset, and carrier phase, respectively. T_s is the sampling period, which is equal to $1/f_s$, where f_s is the sampling frequency. $f_{\mathrm{IF},L1}$ and $f_{\mathrm{IF},L5}$ are the IF values of the RFE for GPS L1 C/A and L5 signals, respectively. A_{L1} and A_{L5} are the signal powers of received GPS L1 C/A and L5 signals, respectively. GNSS receiver algorithms are responsible for the synchronization of the received signal and the locally generated signal to demodulate the navigation data (d_{L1} and d_{L5}) according to a two-stage architecture made of acquisition and tracking. $\eta_{L1,\mathrm{IF}}(nT_s)$ and $\eta_{L5,\mathrm{IF}}(nT_s)$ are the down-converted and filtered noise components that are assumed to be additive white Gaussian noise.

After having mentioned the general signal structures of L1 C/A and L5, both acquisition and tracking structures are explained in the following sections.

IV. ACQUISITION ARCHITECTURES

At the acquisition stage, the objective is to process the incoming digitized signals to find out all the visible satellites. Rough synchronization of the locally generated signal with the incoming one is performed and the estimated Doppler frequency (f_D) and code phase (τ) values of all the acquired satellites are fed to the tracking stage.

Fig. 4 shows the general structure of a coherent acquisition using a coherent integration time equal to one primary code period and K noncoherent accumulations. In the L5 acquisition case, the input signal can be correlated with the pilot or the data channel. In case of data-pilot acquisition, the number of correlators in Fig. 4 must be doubled in number in order to include the processing of both the data and pilot channels in two separate channels. Although, it will cause an increase in the computational burden, it will increase as well the available signal power. In our tests of the L5 signal, we process the signal by correlating with only the pilot local-signal in order to exploit the advantage of the absence of the navigation data.

At the acquisition stage, different locally generated Doppler frequency (f_D) and code delay (τ) values are tested to estimate the delay and Doppler shift of the incoming signal. For all possible combinations (τ, f_D), the correlator outputs in Fig. 4 for the pilot and the data channel acquisitions during the coherent integration in the case of no sign transition are expressed as [30]

$$Y_{I,p_k}(\tau,f_D)\approx\sqrt{\frac{C}{4}}R(\Delta T_k)\frac{\sin(\pi\Delta F_kT_c)}{\pi\Delta F_kT_c}\cos(\Delta\theta_k)+\eta_{I,p_k} \tag{7}$$

$$Y_{Q,p_k}(\tau,f_D)\approx\sqrt{\frac{C}{4}}R(\Delta T_k)\frac{\sin(\pi\Delta F_kT_c)}{\pi\Delta F_kT_c}\sin(\Delta\theta_k)+\eta_{Q,p_k} \tag{8}$$

$$Y_{I,d_k}(\tau,f_D)\approx\sqrt{\frac{C}{4}}d_kR(\Delta T_k)\frac{\sin(\pi\Delta F_kT_c)}{\pi\Delta F_kT_c}\cos(\Delta\theta_k)+\eta_{I,d_k} \tag{9}$$

$$Y_{Q,d_k}(\tau,f_D)\approx\sqrt{\frac{C}{4}}d_kR(\Delta T_k)\frac{\sin(\pi\Delta F_kT_c)}{\pi\Delta F_kT_c}\sin(\Delta\theta_k)+\eta_{Q,d_k} \tag{10}$$

where subscripts d and p correspond to the data and the pilot channels, respectively. Subscript k is the accumulation number that corresponds to the duration between kT_c and $(k+1)T_c$, where T_c corresponds to the coherent integration time interval. $R(\Delta T_k)$ is the normalized kth cross correlation between the incoming and the generated codes, ΔT_k is the kth sampled code delay difference between the generated local one (τ) and the incoming one (τ_0). ΔF_k is the kth frequency difference between the locally generated carrier and the incoming one: $\Delta F_k = f_0 - f_D$. $\Delta\theta_k$ is unknown residual phase value. η_{I,p_k}, η_{Q,p_k}, η_{I,d_k}, and η_{Q,d_k} are kth Gaussian noise terms. d_k is the sign of the kth navigation data bit which is only included in the data-channel for GPS L5 and L1 C/A signal.

Since L1 C/A signal and both carrier components of GPS L5 signal are BPSK modulated by different sequences of bits, (9) and (10) are valid for GPS L1 C/A. Having obtained the correlations in each branch, the test statistics,

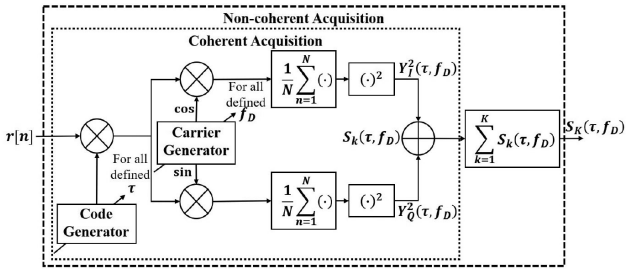

Fig. 4. GPS signal acquisition block for coherent and noncoherent cases.

namely, the cross ambiguity function (CAF), is computed by squaring and summing each result so as to remove the dependence on the unknown phase residual ($\Delta\theta_k$)

$$S_k(\tau, f_D) = Y^2_{I,p/d_k}(\tau, f_D) + Y^2_{Q,p/d_k}(\tau, f_D) \approx \left|\sqrt{C/4}\, R(\Delta T_k)\,\mathrm{sinc}(\pi\,\Delta F_k T_c) + \eta_{IQ_k}\right|^2 \quad (11)$$

where η_{IQ_k} is the resulting noise contribution. By employing K independent correlations, noncoherent acquisition method can be implemented and the test statistics is changed to $S_K(\tau, f_D)$

$$S_K(\tau, f_D) = \sum_{k=1}^{K} S_k(\tau, f_D). \quad (12)$$

One of the performance comparison parameters that is taken into account in this article is the peak-to-floor ratio. It is computed as by considering the test statistics parameters in (11) or (12)

$$\alpha_{\max} = 20\log_{10}\left(\frac{\max(S_K)}{\max(S_{\text{floor}})}\right) \quad (13)$$

where S_{floor} is the set of CAF values outside of the main peak.

A. Acquisition Methods

In this article, four L5 and three L1 C/A acquisition methods are implemented and compared in terms of probabilities of detection/false alarm, peak-to-noise floor ratios, and acquisition time duration. Although Fig. 4 shows the time-domain implementation of the acquisition structure with cross correlations, in our implementation, the cross correlation of the incoming and generated signal is computed through fast Fourier transform-based correlation.

The first applied technique (*Method-A*), coherent channel combining, was originally proposed in [10], [11], and [31], and it has been implemented for $T_c = 1$ ms with K noncoherent accumulations in order to be able to neglect the presence of the NH codes. The choice of $T_c = 1$ ms is due to the fact that both primary spreading code and one NH bit are 1 ms long and that we want to avoid a potential bit transition that could lead to a degradation when finding the peak in the acquisition.

The second technique considered (*Method-B*) is the zero-padding algorithm presented in [12] and [30]. This algorithm takes into account the degradation effect of the possible presence of NH-bit transitions. These sign transition issues are generally solved by using extended local replica with zero-padding [30]. Zero padding acquisition is implemented by circularly correlating two code periods of the incoming signal with one primary code period of locally generated code appended by one primary code period of zeros. This method produces two peaks in the output and it is possible to find a degraded peak in the second half of the correlation due to NH bit transition [30]. Although, this method increases the computational load due to the augmented FFT length compared to Method-A, it also increases the chance of acquiring the satellite signal considering the effect of NH bit transitions. However, selecting FFT length for zero padding is a design parameter to consider in terms of computation issues and an interested reader can find useful materials in [32].

As third strategy (*Method-C*), $T_c = 20$ ms with noncoherent accumulations on the data-less channel is implemented. This method has been proposed in different configurations for L5 signals in [11] and [12]. Such an integration is highly effective for low signal-to-noise ratio conditions; however, it is computationally heavy with respect to the previous two aforementioned methods. Moreover, since L5 signal includes secondary NH codes (differently from L1 C/A), a misalignment of the NH code could cause false peaks in the L5 CAF output. In the scientific literature, in order to obtain a perfect synchronization with NH codes, a couple of techniques have been proposed. In the first approach, it is suggested to employ consecutive acquisitions with short integration time to detect the NH bit transitions in a tree data structure [33] or to eliminate secondary code ambiguity based on multihypothesis in Galileo primary code acquisition [34]. The aforementioned methods described in [33] and [34] that apply possible secondary code combinations in an evolutionary tree structure are improved by coherently extending the integration time by testing all possible combinations through the m-sequence method [35] and coherently accumulating the correlation values obtained over shorter length sequences [36]. In the second approach, the synchronization is obtained by implementing correlations with secondary codes [37] or by combining those secondary correlations [38] to reduce the number of possible secondary code delays and complexity. We followed the first approach by applying an exhaustive search considering all possible combinations in a hierarchical tree structure. At first consecutive zero-padding acquisitions over primary code lengths of the incoming signal are performed by including both first and second half of the correlation output. The peaks of CAF are evaluated to detect the correlation peaks that are distributed along the Doppler axis due to sign transitions. The NH code phase is obtained by exhaustive testing. Later, by generating the full-length NF code with the known phase, Method-C is applied. In Method-C, while T_c can be chosen as 20 ms for L5 pilot channel, it is set to 10 ms for L1 C/A due to possible data-bit transitions. Between two consecutive 10 ms data intervals,

TABLE II
Specifications of the Acquisition Methods

		Method A	Method B	Method C	Method D
Coh. Integ. Time [ms]	L5	1	1	20	2
	L1 C/A	1	1	10	-
Number of Non.Coh Accumulations		3	3	3	1

TABLE III
Performance Metrics of the Acquisition Methods

		Method A	Method B	Method C	Method D
Peak-to-floor ratios [dB]	L5	23.12	25.55	39.5	$14.25-17.81$
	L1 C/A	19.79	21.01	33.1	-
Acq. time per SV* ∼Comput. Load	L5	t_5	$2.5t_5$	$14t_5$	$1.6t_5$
	L1 C/A	t_1	$2t_1$	$8.25t_1$	-

*Front-end sampling frequencies for L1 and L5 signals are 5 and 30 MHz, respectively. Since the number of the samples for the chips are different, two different time-measurement parameters (t_5 and t_1) are defined, obtaining that $t_5 = 3.65t_1$.

at most one navigation data bit phase transition exists and one of these has no data bit phase transition [39].

In the last considered option (*Method-D*), instead of detecting all the sign-transitions of the NH codes, we applied the differentially coherent channel combining with sign recovery algorithm whose implementation details are available in [5] and that has a lower computational complexity. The motivation of this algorithm is to decrease the effect of the NH bit sign-transition by combining the information of both cases, where the NH bits are 1 and 0 for two consecutive 1 ms intervals of data. Since the motivation comes from the existence of the secondary codes, this method has not been applied to the L1 C/A signal.

Table II summarizes the parameters of the implemented acquisition methods for L1 C/A and L5. The first analysis has been performed under nonscintillated conditions.

In Table III, the results obtained for the performance metrics are given. The test was realized by processing the data that belong to 8 May 2016 [see Fig. 2(a)]. By considering the first 3 min interval of the data in which the scintillation has not started yet, the peak-to-floor ratios are computed for each method. The results in Table III are the mean values obtained. Moreover, computed mean C/N_0 values for GPS L5 and L1 C/A signals are 51 and 48 dBHz, respectively. As it can be seen in Table III, when the coherent integration time is extended, an improvement in the peak-to-noise ratio is observed, but at the same time, an increment of the computational load, which is the consequence of the time dedicated by the receiver to the acquisition stage, is observed. The number of noncoherent accumulations is decided experimentally by trying to make it as lowest as possible and at the same time having an acceptable peak-to-floor ratio.

In Table III, there are two different values for Method-D as being different from the other methods. The difference between the two cases corresponds to the situations, where

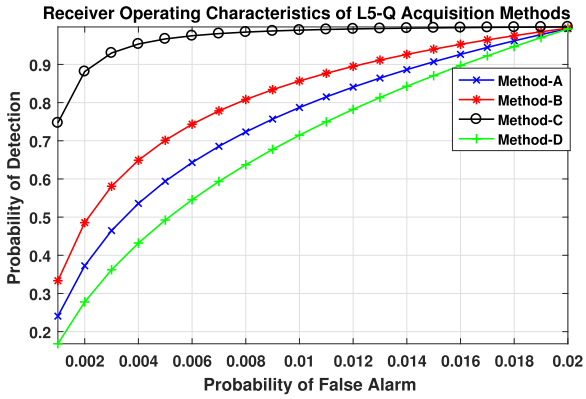

(a)

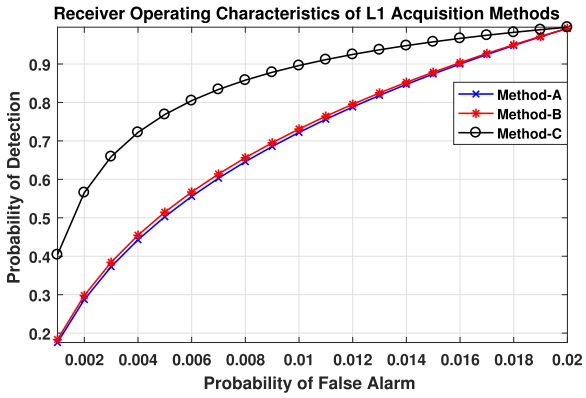

(b)

Fig. 5. ROC curves of the implemented methods for GPS L1 C/A, L5 signals under no-scintillation. (a) GPS L5 pilot signal ($C/N_0 = 51$ dBHz). (b) GPS L1 C/A signal ($C/N_0 = 48$ dBHz).

the NH bit sign transition occurred and not occurred in consecutive two 1 ms intervals. The number of noncoherent accumulations is set to 1 to make it simpler, otherwise, the number of different peak-to-noise ratio values increase depending on the number of possible NH bit combinations. Therefore, it is inferred that the performance of Method-D is dependent on the observation of NH bit change in the considered 2 ms coherent integration time interval.

Furthermore, Fig. 5(a) and (b) shows the receiver operating characteristics (ROC) curves, which are the plots of the probability of detection (P_D) versus the probability of false alarm (P_{FA}) at the search space level, of the implemented acquisition algorithms for GPS L5 pilot and GPS L1 C/A signals, respectively. In fact, for example in case of noncoherent acquisition, probability of false alarm and probability of detection can be written as [40]

$$P_{FA,K}(\beta) = \exp\left(-\frac{\beta}{2\sigma_n^2}\right)\sum_{i=0}^{K-1}\frac{1}{i!}\left(\frac{\beta}{2\sigma_n^2}\right)^i \tag{14}$$

$$P_{D,K}(\beta) = \mathrm{Q_K}\left(\sqrt{\frac{K\lambda}{\sigma_n^2}}, \sqrt{\frac{\beta}{\sigma_n^2}}\right) \tag{15}$$

where β is the detection threshold and $\mathrm{Q_K}(a, b)$ is the generalized Marcum-Q function. λ and σ_n^2 are computed

from CAF outputs [7], [10], [40]. λ is the noncentrality parameter of the test statistics $S_K(\tau, f_D)$ that is a noncentral χ^2 random variable with $2^{\sim}K$ degrees of freedom when the local signal is aligned with the received signal [5]. σ_n^2 is the variance of the in-phase ($Y^2_{I,p/d_k}$) and quadrature-phase ($Y^2_{Q,p/d_k}$) correlator outputs. Moreover, the successful acquisition of a satellite signal is declared when $S_K(\tau, f_D)$ passes the decision threshold (β) for a value of τ and f_D. ROC curves are then obtained (varying β) for each methods at each second (i.e., for the C/N_0 experienced at that epoch).

As it can be seen in Fig. 5, the performance of the Method-A is not remarkably better than the Method-D for GPS L5 pilot channel. However, the zero-padding method (Method-B) is slightly better than the Method-A. Moreover, as expected, extending the integration time (Method-C) provides an improvement in the performance. The performance improvement in the probability of detection of GPS L5 signal compared to the L1 C/A signal is induced from 3 dBHz difference in the signal-to-noise ratio.

After having analyzed the performance of the implemented methods with the nonscintillated data, we studied the scintillation effect on the L5 and L1 C/A acquisition stages as presented in the following section.

B. Performance Comparison of the Acquisition Methods

After the description of acquisition method, we have tested them, at first, on the datasets that were collected on May 8 and August 17, 2016 [Fig. 2(a)-(b)] in the Antarctic stations SANAE IV and that are affected only by strong phase scintillation. The estimated mean C/N_0 values for the datasets are 51 and 46 dBHz for GPS L5 signals, respectively. However, for GPS L1 C/A signals, they are estimated as 48 and 44 dBHz, respectively. In the analysis, we run the acquisition algorithms (with $P_{\text{FA}} = 0.001$) every second for the whole data collection and then we have checked the amount of time we failed to acquire the satellites (i.e., PRN3 and PRN9) affected by strong phase scintillation. This process is repeated for all the acquisition methods for GPS L5 and L1 C/A signals. It is observed that during the phase scintillation events the signal is acquired all the time for all the methods. This result is not surprising, since the phase scintillation has less impact on the acquisition stage. It points out that the rate of phase changes occurred during the phase scintillation events stays quite constant over the integration time or this effect is minimal in the acquisition process. In order to analyze the effects of the phase scintillation, the changes in the ROC curves due to scintillation are also analyzed.

Such ROC curves are computed by employing the acquisition results at each second. At every second we have detected when the scintillation is strong ($\sigma_\phi > 0.7$) or no-scintillation exists ($\sigma_\phi < 0.2$). In this way, it has been possible to make a statistical and fair comparison between the case of no-scintillation and phase scintillation. For the two cases, the mean P_D values are computed for each given P_{FA} values. Then, the differences between the mean P_D values of no-scintillation and scintillation cases for the same

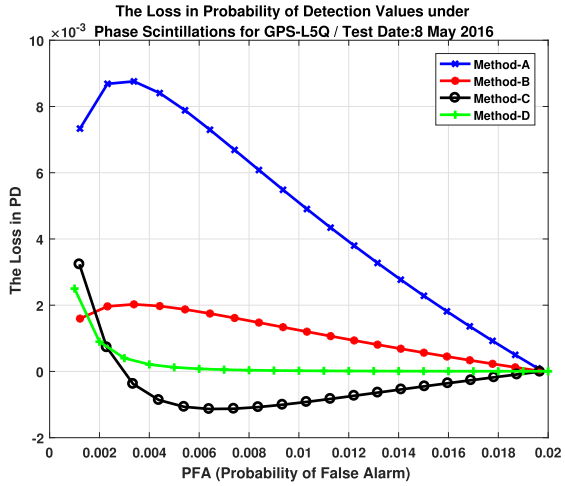

(a)

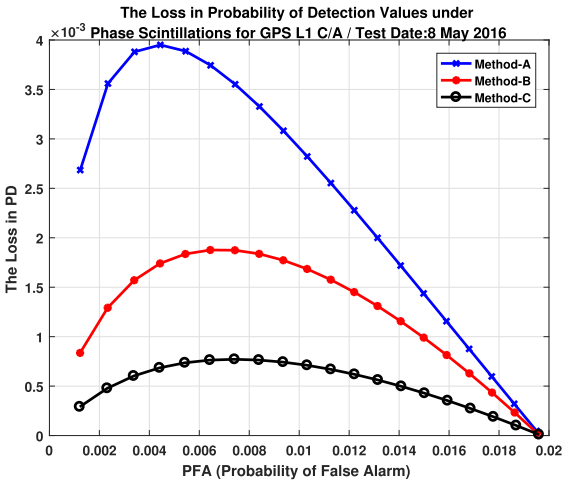

(b)

Fig. 6. Loss in PD of the acquisition methods for GPS L1 C/A, L5 signals under phase scintillation—May 8, 2016. (a) GPS L5 pilot signal. (b) GPS L1 C/A signal.

P_{FA} values are computed. This procedure is repeated for the two datasets.

Figs. 6 and 7 show the loss in the P_D values of the aforementioned L5 and L1 C/A acquisition methods under phase scintillations for the two events. It is observed that, in case of strong scintillation, we have a loss in P_D of only 0.013–0.002 with respect to the case without scintillation. Whereas the ROC curves in Fig. 5 belong to a timestamp, Figs. 6 and 7 cover a duration during which different levels of phase scintillation exist, and the C/N_0 changes in time as it might be expected. Therefore, due to its experimental nature in which the data are analyzed for different levels of scintillation, any conclusion related to shapes of curves would be misleading except the comparison of the loss in P_D among the methods. This is why the analysis results are limited to inferring the loss in P_D of the acquisition methods under phase scintillation.

In the second test, the data that were collected on September 13, 2017 in Brazil have been used. In this event, phase scintillation is mixed with amplitude scintillation.

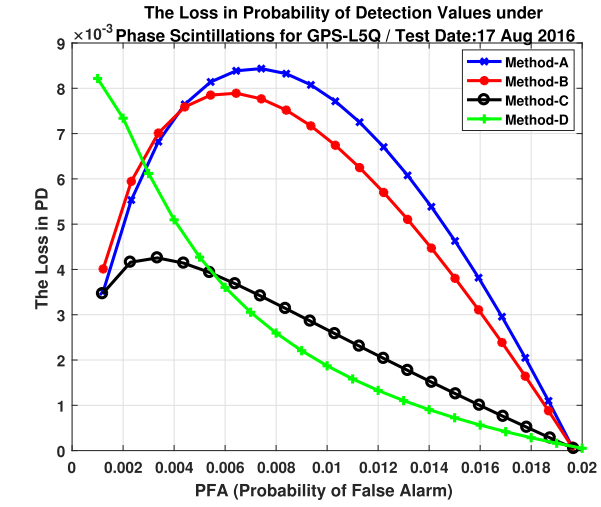

(a)

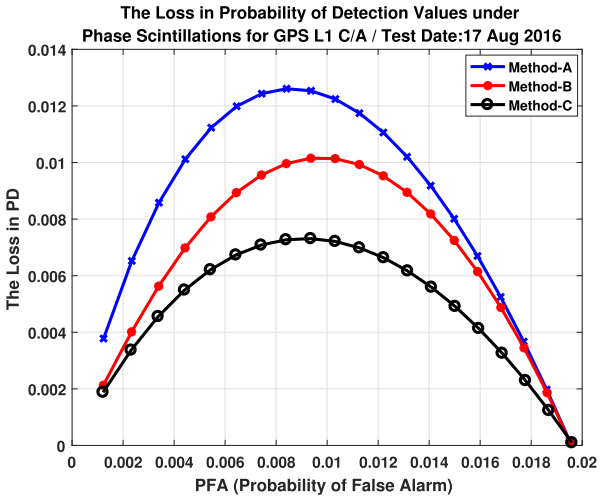

(b)

Fig. 7. Loss in PD of the acquisition methods for GPS L1 C/A, L5 signals under phase scintillation—August 17, 2016. (a) GPS L5 pilot signal. (b) GPS L1 C/A signal.

TABLE IV
Percentages of Successful Acquisition Times Under Amplitude and Phase Scintillation Event

	Method A	Method B	Method C		Method D
	T=1 ms $K=3$	T=1 ms $K=3$	T=10 ms $K=3$	T=20 ms $K=3$	T=2 ms $K=1$
L5-Q	79.96 %	88.73 %	98.55 %	98.90 %	64.49 %
L1 C/A	57.26 %	59.71 %	99.78 %	-	-

*T is the coherent integration time and K is the number of non-coherent accumulations.

Fig. 8 shows the acquisition performance of the methods during 45 min length data. The percentages of successful acquisition times (with $P_{\text{FA}} = 0.001$) are computed and summarized in Table IV.

As it can be seen in Table IV, the acquisition performance of the L5 outperforms L1 C/A in both Method-A and Method-B. However, as mentioned in Section III, the signal structures and transmitted power are different in L1 C/A and L5, respectively. C/N_0 values of GPS L5 signals are higher than GPS L1 C/A signals. On the contrary, the scintillation is stronger in GPS L5 signal than GPS L1 C/A signal as it can be seen in Figs. 2(a) and (b) and 3(a) and (b). At the same time, it is observed that Method-C, outperforms the other methods in both cases.

Moreover, so as to compensate the C/N_0 difference between GPS L1 C/A and L5 signals and also to see whether performance difference is caused by the signal level difference, we provide extra gain to L1 C/A signal processing. If the integration time is extended to 2 ms, theoretically, an additional 3 dB coherent integration gain is obtained, and in this case, it is expected that L1 C/A performance could get better than L5. As expected, it is observed that for 2 and 3 ms coherent integration time implementation for GPS L1 C/A, the percentages of successful acquisition times reach up to 89.74–95.18 %. However, instead of increasing the coherent integration time of L1 C/A acquisition method, if the number of noncoherent accumulations is increased to $K = 3$ and $K = 7$ for Method-A, it is observed that the percentages of successful acquisition times increase to 74.79 and 77.16 %, respectively.

Summarizing, it is observed that while phase scintillation is not at the level to prevent the acquisition of the signal, strong amplitude scintillation can prevent the acquisition of the signal. In that case, extending integration time can be a solution, and Method-C performs best among the other methods.

V. TRACKING ARCHITECTURES

In a GNSS receiver, after having obtained the rough synchronization of code phase and Doppler frequency of the acquired satellite signals, the values are fed to the tracking stage for code and frequency estimates refinement. In the following of this article, we limit our analysis to the carrier tracking, whose objective is to wipe off the carrier by generating a perfectly aligned one. Because carrier tracking is so susceptible to the scintillation due to PLL's stringent tracking threshold the equatorial phase scintillation adversely affects the operation of carrier tracking leading to cycle slips and complete loss of carrier lock.

A. Overview of Carrier Tracking Method

The general structure of the carrier tracking loop is given in Fig. 9. While tracking the carrier signal, the spreading code of the incoming signal is tried to be aligned with the locally generated code at the same time. The aim is to have all the power in the in-phase (I) branch. In principle, the operation and correlator outputs are the same as in the architecture of Fig. 4. In this case, the carrier phase error is minimized. This is possible when the correlation value in the in-phase branch (I_k) is maximum and in the quadrature-phase branch (Q_k) is zero.

In Fig. 9, the $c_p[n]$ is the prompt spreading code generated at the code tracking loop and the alignment includes a

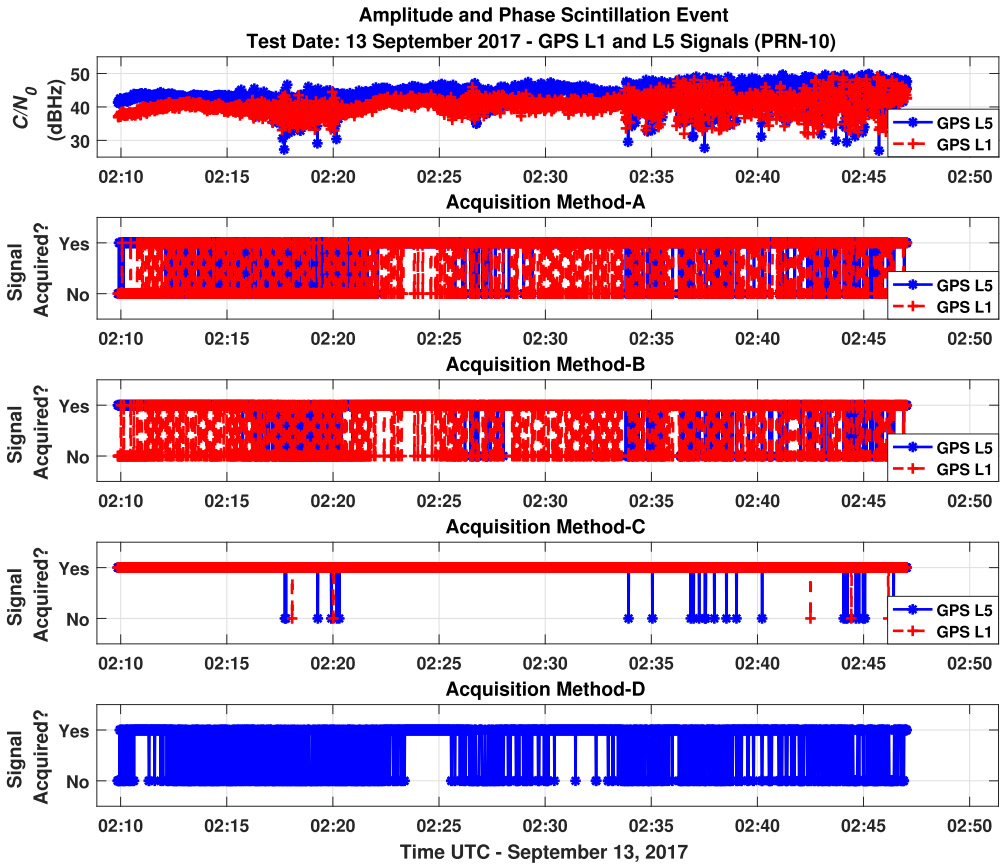

Fig. 8. Performance comparison of GPS L1 C/A, L5 signal acquisition methods under amplitude and phase scintillation—test date: September 13, 2017.

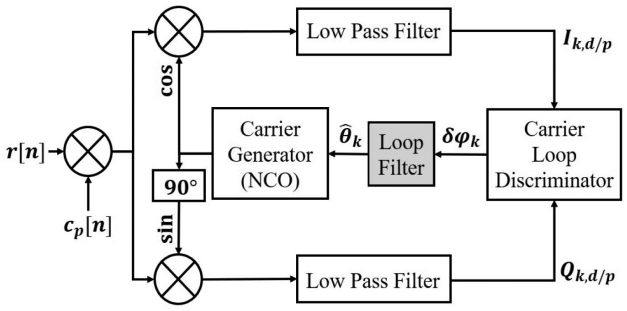

Fig. 9. Signal carrier tracking block diagram.

code delay estimation error ($\delta\tau$), which is also included in the tracking correlator output equations

$$I_{k,p} = A_k R_k(\delta\tau)\frac{\sin(\pi T\delta f_k)}{\pi T\delta f_k}\cos(\delta\varphi_k) + \eta_{I,p_k} \quad (16)$$

$$Q_{k,p} = A_k R_k(\delta\tau)\frac{\sin(\pi T\delta f_k)}{\pi T\delta f_k}\sin(\delta\varphi_k) + \eta_{Q,p_k} \quad (17)$$

$$I_{k,d} = A_k R_k(\delta\tau)d_k\frac{\sin(\pi T\delta f_k)}{\pi T\delta f_k}\cos(\delta\varphi_k) + \eta_{I,d_k} \quad (18)$$

$$Q_{k,d} = A_k R_k(\delta\tau)d_k\frac{\sin(\pi T\delta f_k)}{\pi T\delta f_k}\sin(\delta\varphi_k) + \eta_{Q,d_k} \quad (19)$$

where subscripts d and p correspond to the data and the pilot channels, respectively. $I_{k,d/p}$ and $Q_{k,d/p}$ are in-phase and quadrature correlator outputs, respectively. R is the correlation of the locally generated prompt replica code with the incoming code, d_k is the polarity of the kth navigation data-bit when data channel is considered, δf is the frequency estimation error, and $\delta\varphi_k$ is the average carrier phase estimation error over the coherent integration time (T). After the loop filter, which reduces the noise, A is the carrier amplitude in one branch and η_{I,p_k}, η_{Q,p_k}, η_{I,d_k}, and η_{Q,d_k} are independent Gaussian noise terms. As shown in Fig. 9, a numerically controlled oscillator (NCO) generates a sinusoid of which phase $\widehat{\theta}_k$ is related to filtered discriminator output ($\delta\widehat{\varphi}_k$). $\delta\varphi_k$, the average carrier phase error, is the difference between the one estimated by NCO ($\widehat{\theta}_k$) and the phase of the incoming signal (θ_k).

When an amplitude scintillation occurs, the amplitude of the correlator outputs ($I_{k,d/p}$) is reduced and it causes a lower carrier-to-noise (C/N_0) ratio hindering a receiver's ability to track the signal. On the contrary, phase scintillation not only introduces extra noise to the estimation of the carrier phase error ($\delta\varphi_k$) but also causes deep fadings because of the destructive interference resulting in the loss of lock of the signal. In order to be able to cope with the fading and abrupt phase changes of the scintillation effects, various loop filters have been proposed in the literature. In this section, by

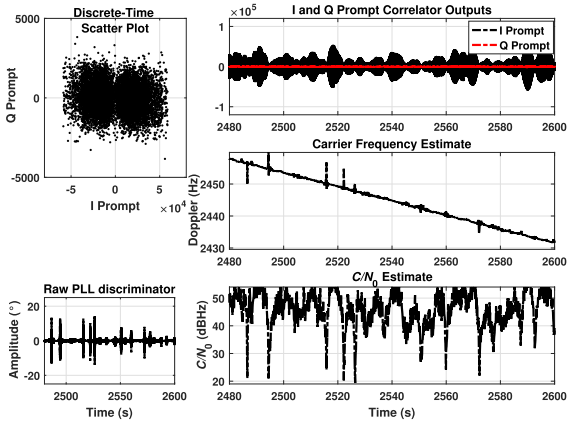

(a)

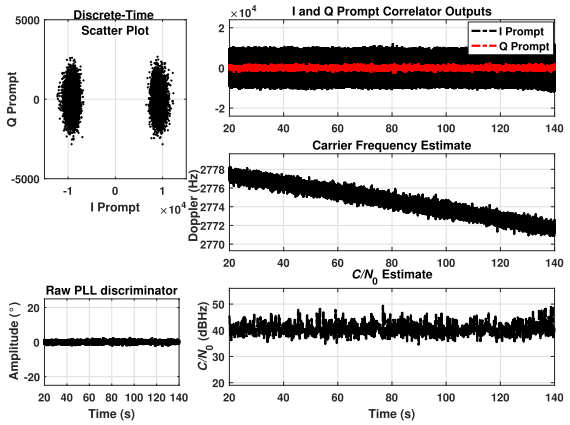

(b)

Fig. 10. Comparison of the tracking observables and internal parameters for L5 data channel under strong scintillation and no-scintillation—test date: September 13, 2017. (a) GPS L5 data channel outputs with second-order PLL, $B_n = 10$ Hz, $T = 10$ ms—under strong scintillation. (b) GPS L5 data channel outputs with second-order PLL, $B_n = 10$ Hz, $T = 10$ ms—no-scintillation.

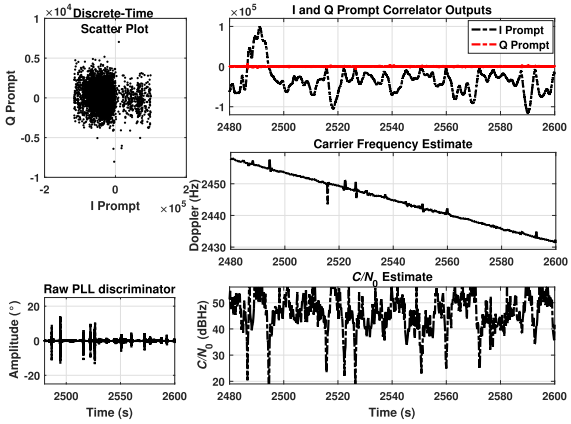

(a)

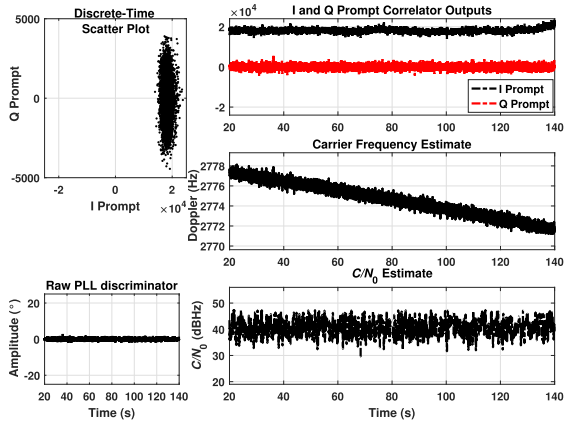

(b)

Fig. 11. Comparison of the tracking observables and internal parameters for L5 quadrature channel under strong scintillation and no-scintillation—test date: September 13, 2017. (a) GPS L5 pilot channel outputs with second-order PLL, $B_n = 10$ Hz, $T = 20$ ms—under strong scintillation. (b) GPS L5 pilot channel outputs with second-order PLL, $B_n = 10$ Hz, $T = 20$ ms—no-scintillation.

employing traditional loop filter architectures (PLL, frequency lock loop, delay lock loop) [41], [42] and KF-based carrier tracking [43], [44], we evaluate and compare the tracking performances of GPS L1 C/A and L5 signals. For the state-space design application of PLL design, three-state KF in which the output of the discriminator is used to map the correlator outputs for the estimation of state errors in the measurement model is applied [43].

B. Performance Comparison of the Tracking Methods

To have robust architectures optimized to operate in a harsh ionospheric environment, first PLL tracking loops are tested by considering the different choices for the loop filter order (second or third), the coherent integration time (T), and the carrier noise bandwidth (B_n). The order of the filter and noise bandwidth determine the loop filter's response to signal dynamics and in PLL loop filter design there is also a tradeoff in the decision of T and B_n parameters [41].

Figs. 10–12(a) and (b) show the changes in the values of correlator outputs ($I_{k,d/p}$ and $Q_{k,d/p}$), raw PLL discriminator output ($\delta\varphi_k$), C/N_0 and carrier frequency estimations during the occurrence of scintillation and no-scintillation activities for GPS L5 data, pilot channels and GPS L1 C/A signal. As it can be seen in Figs. 10–12(a) and (b), the amplitude of the prompt correlator output ($I_{k,d/p}$) both increases and decreases during the scintillation event. Because the diffracted signals interfere with the actual signal and they are added to the actual signal both constructively and/or destructively that yields to alternately both attenuation and strengthening in the signal amplitude and C/N_0 values measured by the user [45].

The data that were collected on September 13, 2017 are used for the analysis in this section. In the analysis shown in the figures, the PLL design parameters $B_n = 10$ Hz, $T = 10$ ms, and $T = 20$ ms are selected for GPS L5 and GPS L1 C/A signals, respectively. Furthermore, at the same conditions, a KF-based tracking, which provides more flexibility thanks to a time-varying bandwidth and gain, has

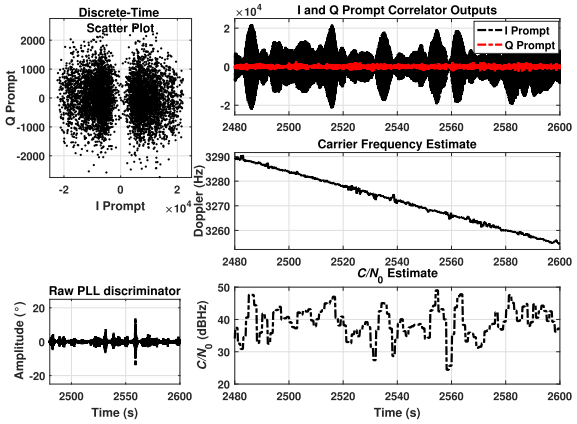

(a)

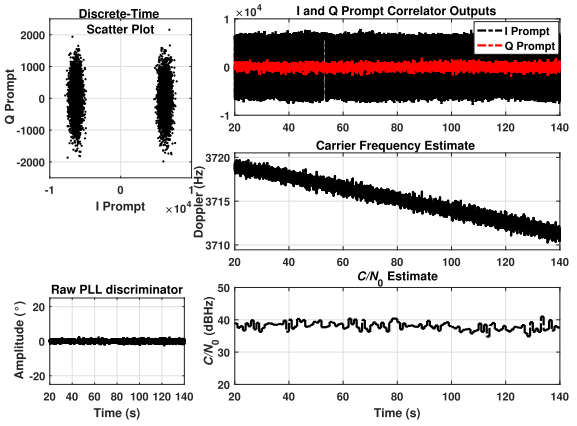

(b)

Fig. 12. Comparison of the tracking observables and internal parameters for L1 C/A signal under strong scintillation and no-scintillation—test date: September 13, 2017. (a) GPS L1 C/A signal outputs with second-order PLL, $B_n = 10$ Hz, $T = 20$ ms—under strong scintillation. (b) GPS L1 C/A signal outputs with second-order PLL, $B_n = 10$ Hz, $T = 20$ ms—no-scintillation.

been evaluated and compared in terms of the residual effects on the receiver observables and internal parameters in the following sections.

1) *Standard Deviation of Doppler Estimations:* We try to find the best PLL parameters to be able to track the Doppler frequency accurately. Doppler shift measurements allow us to compare the tracking robustness in the presence of scintillation effects. Figs. 10–12(a) show 120 s portion of the Doppler estimates of the processed data, which experiences both strong amplitude and phase scintillation. By applying different choices of the loop orders, bandwidth (B_n) and integration time (T), the effects of the PLL parameters on the tracking stage under scintillation have been analyzed. In the analysis, while the extended integration time is set to $T = 10$ ms in the L5 data channel by considering the data bit interval, in the L5 quadrature (dataless) channel the integration time is extended to $T = 20$ ms. Moreover, so as to provide a perceptive comparison in terms of the effect of noise bandwidth, commonly used bandwidths with 5 Hz increments are included in the analysis. Due to scintillation an increment of the standard deviation of Doppler measurements can be observed with different settings of tracking parameters.

To have better comparison, the maximum values of the standard deviations of the Doppler measurements, each value computed on a nonoverlying block of 100 ms, have been estimated and all the results are summarized in Tables V and VI for scintillation and no-scintillation cases, respectively. It is observed that processing the L5 data or the pilot channel with $T = 1$ ms has no advantages over each other, as expected. Moreover, although we do not observe remarkable performance difference with using L1 C/A or L5 signals in case of $T = 1$ ms, it is clear that the performance degrades with increasing B_n values, which means that the noise level can be reduced by reducing the noise bandwidth. On the contrary, when the coherent integration time is extended to 10 ms for the L5 data channel and 20 ms for the L5 pilot channel and GPS L1 C/A signal, the latter shows a lower error in the Doppler measurement for low value of bandwidth (i.e., <10 Hz).

As it can be seen in Table V, there is a sharp increase in the values due to the change of B_n from 15 to 20 Hz, especially in the case of $T = 20$ ms. Since the product B_nT increases, the true noise bandwidth tends to be larger than the aimed value and hence the loop filter becomes unstable [41]. Moreover, although the second order is unconditionally stable, the third order can be unstable under fluctuating C/N_0 values due to scintillation. In the cases of third-order loop filter with $B_n = 15$ and 20 Hz and $T = 20$ ms, tracking is completely is lost after some time.

2) *Phase Error:* A PLL discriminator, shown in Fig. 9 carrier tracking structure, computes the difference between the phase of the incoming signal and the locally generated signal. Here, we use two-quadrant Costas PLL discriminator, which outputs the phase error as

$$\delta\varphi_k = \tan^{-1}\left(\frac{Q_{k,d/p}}{I_{k,d/p}}\right) \tag{20}$$

where $(\delta\varphi_k)$ is the estimated carrier phase error over the integration time (T).

Figs. 10 and 11(a) and (b) show the tracking results of the processed L5 data and pilot signals. The tracking results of the L5 data channel show similar characteristics with L1 C/A shown in Fig. 12. Since L1 C/A and L5 data signals have 180° phase ambiguity due to the navigation data, NCO creates two different cloud of points that are visible in Figs. 10 and 12(b) in the discrete-time scatter plot. However, the tracking results of the L5 pilot [see Fig. 11(b)] channel with extended integration time (20 ms) differs from them in terms of the phase measurement. In both cases, the amplitude scintillation causes the elongation of the clouds due to the occurrence of the power fades, which can be clearly seen in the IQ prompt correlator in time graphs. When the two clouds get closer to each other while tracking the L1 C/A and the L5 data-channel signals, it causes an increase in the error with the increase in the

TABLE V
Max Value of the Standard Deviations of the Doppler Measurements [Hz]

			2^{nd} Order PLL				3^{rd} Order PLL			
			Noise Bandwidth (B_n) [Hz]				Noise Bandwidth (B_n) [Hz]			
			5	10	15	20	5	10	15	20
Integ. Time (T)	1ms	L5I	2.16	4.00	6.19	8.34	2.49	4.61	7.28	9.33
		L5Q	2.01	3.97	6.01	8.09	2.26	4.57	7.21	9.23
		L1 C/A	2.19	3.83	6.01	8.39	2.18	4.79	7.49	9.54
	L5I: 10ms	L5I	**1.89**	5.09	7.59	10.85	2.68	5.56	7.75	10.8
	L5Q: 20ms	L5Q	**1.96**	5.64	8.50	14.94	1.98	6.00	9.90	143
	L1 C/A: 20ms	L1 C/A	**1.90**	5.00	7.44	15.55	2.49	5.38	34.2	167

Each std-value corresponds to 100 ms of 3-min long signal record of the strong scintillation event—test date: september 13, 2017.

TABLE VI
Max Value of the Standard Deviations of the Doppler Measurements [Hz]

			2^{nd} Order PLL				3^{rd} Order PLL			
			Noise Bandwidth (B_n) [Hz]				Noise Bandwidth (B_n) [Hz]			
			5	10	15	20	5	10	15	20
Integ. Time (T)	1ms	L5I	0.68	1.38	2.08	2.80	0.78	1.58	2.38	3.19
		L5Q	0.66	1.33	2.01	2.69	0.76	1.51	2.29	3.06
		L1 C/A	0.89	1.82	2.75	3.67	1.02	2.07	3.10	4.16
	L5I: 10ms	L5I	**0.29**	0.65	1.08	1.61	0.32	0.69	1.11	1.69
	L5Q: 20ms	L5Q	**0.28**	0.74	1.85	4.61	0.31	0.82	1.58	2.75
	L1 C/A: 20ms	L1 C/A	**0.39**	0.93	2.17	5.49	0.45	1.03	2.02	3.53

Each std-value corresponds to 100 ms of 3-min long signal record of the no-scintillation event—test date: September 13, 2017.

standard deviation of the phase measurements. Moreover, the abrupt phase changes causing the phase error are seen at the output of the discriminator in the figure. Finally, the trend and the scintillation of the C/N_0 values during the scintillation can be observed in time.

Furthermore, we compared the computed phase error values in the case of both scintillation and normal conditions and we plotted their trend at different C/N_0 values in Fig. 13(a) and (b) for L5 and L1 C/A signals, respectively. The phase error values in Fig. 13 are the mean of the computed values at each 1 dB-Hz intervals. As expected, the phase error is higher at lower C/N_0 values and it decreases with increasing C/N_0. It is inferred that a constant degradation in the accuracy of the carrier phase measurements can be encountered due to scintillation and hence fluctuating C/N_0. It can be observed that the L1 C/A signal tracking provides a phase error that is slightly higher (few degrees) than the one computed for the L5 signal under the same condition of the scintillations, namely when they have the same C/N_0 values. In the L5 case, due to larger fluctuations when C/N_0 goes to lower values, phase error reaches to higher values than observed in L1 C/A. Besides, it is observed that the C/N_0 measurements stay in the limited range without having fluctuation when there is no-scintillation.

Moreover, in the first dataset (May 8, 2016) in which having scintillation signals with only phase variations and no amplitude fading, we also made the same analysis. Phase error values at different C/N_0 values are plotted in Fig. 14. As it can be inferred from Fig. 14, phase changes are not as abrupt as observed in the dataset (September 13, 2017) that is collected in the CRAAM station. We also have good signal-to-noise ratio due to there is no amplitude scintillation and deep fading.

As analyzed up to now, the loop order, the bandwidth (B_n) and the integration time (T) are typically *a priori* set in the PLL structure. In the following sections, in order to evaluate the robustness of a KF-based PLL with respect to a traditional second-order PLL, two parameters have been considered: the phase lock indicator (PLI) and the PLL noise jitter.

3) *Tracking Lock Indicator:* PLI is computed by considering the prompt IQ correlator outputs of the carrier tracking algorithm [46]

$$\mathrm{PLI}_k = \frac{I_{k,d/p}^2 - Q_{k,d/p}^2}{I_{k,d/p}^2 + Q_{k,d/p}^2} \approx \cos(2\Delta\varphi_k) \tag{21}$$

where $\mathrm{PLI} = 0.866$ is taken as the acceptable threshold, which corresponds to $\Delta\varphi = 15^\circ$ as the limit of the phase error in our implementations. The phase error threshold has been decided by considering the results provided for no-scintillation cases in the previous analysis.

In the analysis, the PLI samples, which are less than 0.866 are indicated as loss of tracking points and the number of the samples is used as the performance assessment parameter for the comparison of the different algorithms. Fig. 15 shows the computed PLI values of the L5 data, pilot channels, and L1 C/A signals when the signals experience both strong phase and amplitude scintillations. It is

TABLE VII
PLL and KF-Based Carrier Tracking—Percentages of Unsuccessful Tracking During 3-Min Length Strong Scintillation Event—September 13, 2017

Carrier Tracking	L5-I		L5-Q		L1 C/A	
	$T = 1$ ms	$T = 10$ ms	$T = 1$ ms	$T = 20$ ms	$T = 1$ ms	$T = 20$ms
2^{nd} Order PLL $B_n = 5$ Hz	12.03 %	2.37 %	12.26 %	2.19 %	27.40 %	1.99 %
KF-Based	11.44 %	1.91 %	11.53 %	1.14 %	26.12 %	1.33 %

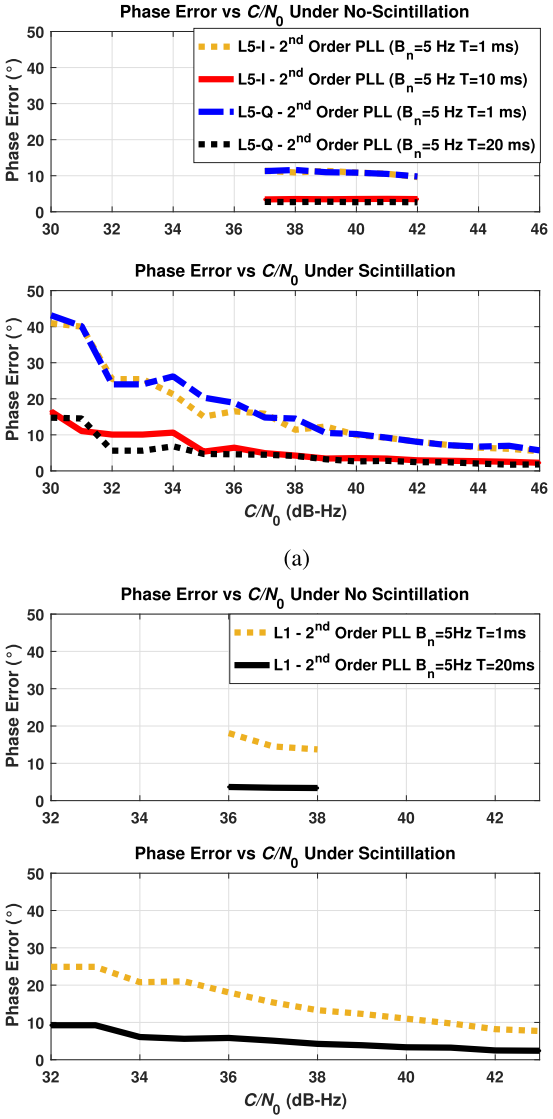

Fig. 13. Phase error versus C/N_0 comparison for L1 C/A, L5 data and pilot channels under scintillation (amplitude + phase) and no-scintillation cases—test date: September 13, 2017. (a) GPS L5 data—pilot signals. (b) GPS L1 C/A signal.

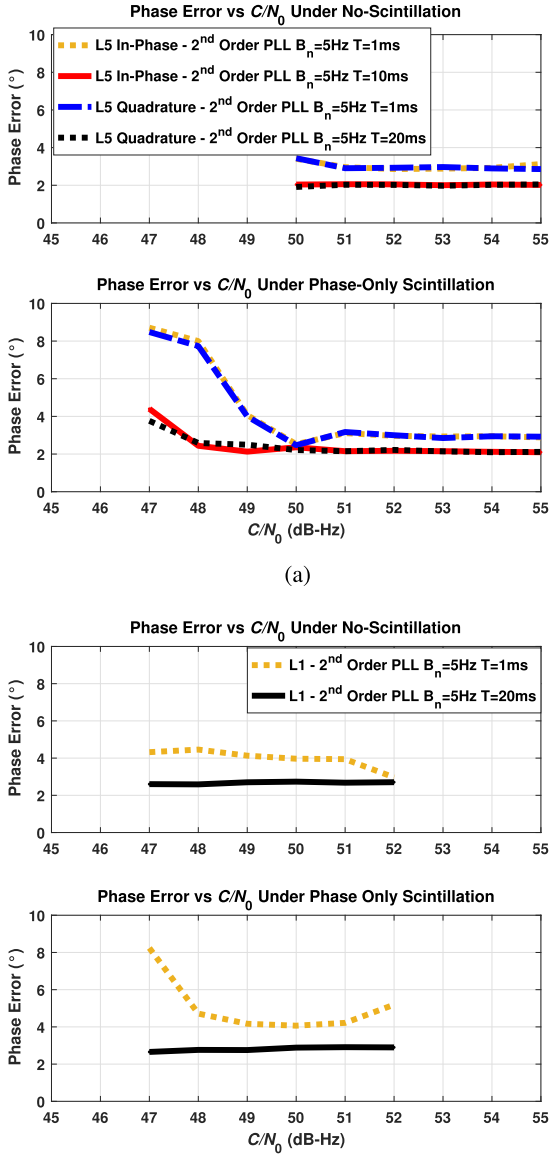

Fig. 14. Phase error versus C/N_0 comparison for L1 C/A, L5 data and pilot channels under phase-only scintillation and no-scintillation cases—test date: May 8, 2016. (a) GPS L5 data—pilot signals. (b) GPS L1 C/A signal.

observed that with short integration time implementation, signal tracking is lost for a long time.

Table VII summarizes the unsuccessful tracking percentages for L5 data-pilot channels and L1 C/A signal with different integration times in 3 min length of the processed data for PLL and KF-based tracking structures. When the integration is extended to $T = 10$ and $T = 20$ ms, the percentages of the loss-of-tracking decrease.

As mentioned, KF-based carrier tracking algorithm outperforms the PLL-based tracking; however, it can also fail under phase scintillation accompanied by strong amplitude

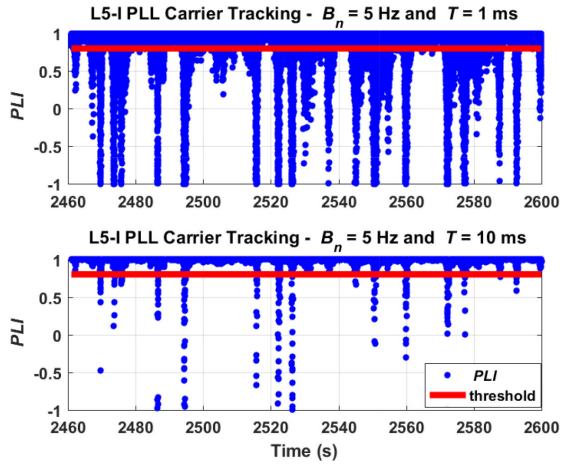

(a)

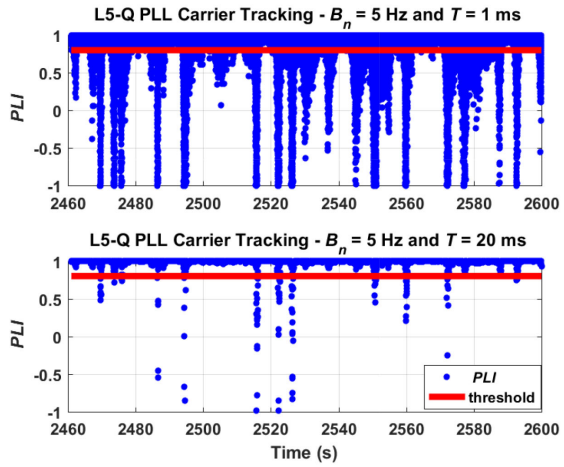

(b)

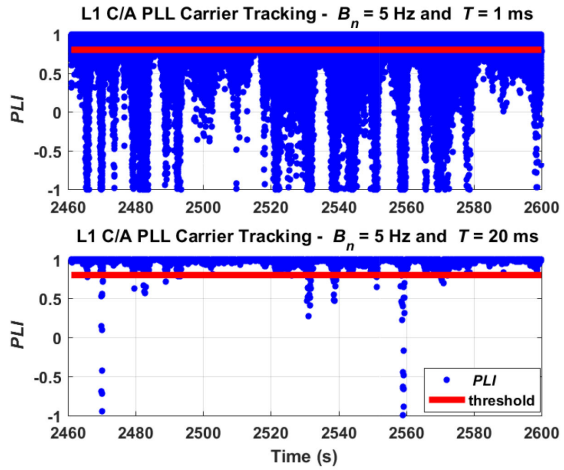

(c)

Fig. 15. PLL carrier tracking—PLI values of L5 data, pilot channels, and L1 C/A signal under strong amplitude and phase scintillations—test date: September 13, 2017. (a) GPS L5 data channel. (b) GPS L5 pilot channel. (c) GPS L1 C/A signal.

scintillation conditions. With KF implementation, we observed that the tracking is improved and the loss-of-tracking percentages decreased for the L5 data, pilot, and L1 C/A signal.

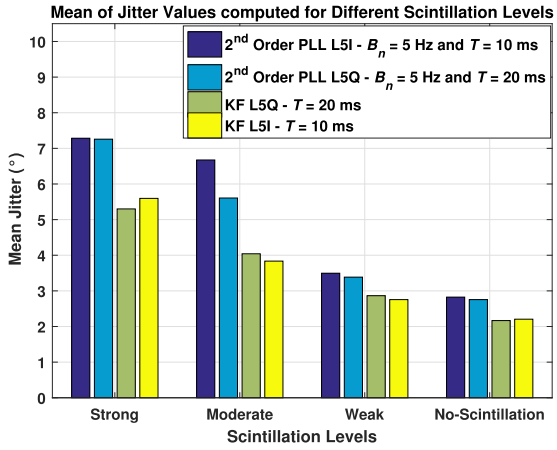

(a)

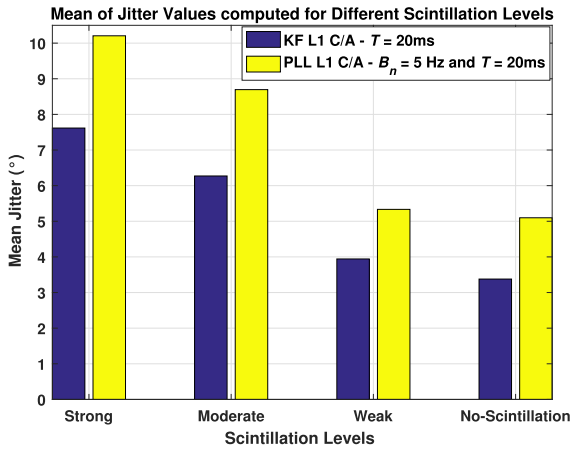

(b)

Fig. 16. Carrier tracking noise jitter of different methods for L5 data, pilot channels and L1 C/A signal—test date: September 13, 2017. (a) GPS L5 signal. (b) GPS L1 C/A signal.

Furthermore, in the first dataset (May 8, 2016) in which having scintillation signals with only phase variations and no amplitude fading, both the traditional PLL and the Kalman-based carrier tracking structure have been used to process the signals. In this case, both PLL and KF-based carrier tracking performed well without experiencing any loss-of-lock. It can also be inferred from Fig. 14 because computed phase error values are not higher than the threshold that is considered for loss of tracking.

4) *Jitter:* Phase jitter is the root sum square of every source of the uncorrelated phase error, such as thermal noise and oscillator noise [41]. The jitter is estimated by computing the standard deviation of the carrier phase tracking error defined in (20) and as the last metric, it has been used for performance comparison [47].

In the analysis, first of all by considering the phase and amplitude indices shown in Fig. 3(a) and (b), the scintillation effect is classified as strong, moderate, weak, and no-scintillation and the starting/ending times are defined for each. For the defined portions-in-time, the phase jitter values are computed for each method and the signal type. Fig. 16 shows the jitter values of the tracking outputs for L5 data, pilot channels, and L1 C/A signal.

It is expected that the L5 pilot channel, which uses a longer integration time and thus gives a higher SNR in output than the L5 data channel, provides better results. As it can be seen in Fig. 16, L5-pilot channel tracking provides better jitter performance than the L5-data channel in both PLL and KF-based tracking methods. Furthermore, KF-based tracking provides improvement compared to the PLL-tracking structure in terms of jitter performance in the case of both L5 and L1 C/A signals. However, it is expected that the GPS L5 signal, whose chipping rate is ten times higher and its power is higher than L1 C/A, provides better results. As expected, tracking of L1 C/A signal experiences higher jitter compared to the L5 signal.

VI. CONCLUSION

In this article, we have reviewed different acquisition techniques and traditional PLL carrier tracking algorithm, and beside PLL, we have also used KF-based carrier tracking algorithm. We have analyzed their performance under strong amplitude and phase scintillations and no scintillation environment by exploiting the real GNSS signals.

Generally speaking, in acquisition, the usage of only one channel for the L5 signal, namely the pilot channel, provides simplicity and reduction in the computational load. In addition, having compared the performance of the algorithms for L5 and L1 C/A in terms of ROC curves, peak-to-floor ratios, the signal acquisition time or computational load, the trade-off between sensitivity and complexity has been provided to evaluate better the performances of the acquisition methods. Concerning the performance under scintillation, under phase-only scintillation, although the signal is acquired all the time, a loss in the probability of detection is computed around $0.013 - 0.002$. Although the phase scintillation is not at the level to prevent the acquisition of the scintillated signal, the phase scintillation accompanied by the strong amplitude scintillation can prevent the acquisition of the signal. In that case, extending the integration time can be considered as a solution and Method-C performs best among the other methods.

Furthermore, different parameter settings of the PLL loop filters and their effects on the receiver tracking performance have been evaluated. With the performance analysis in terms of the residual errors on the receiver observables and internal parameters, it is observed that although L5 signal experiences larger fluctuations under scintillation due to its lower frequency, the tracking outputs of the processed L1 C/A signal have provided more errors, mostly due to lower power with respect to the L5 signal. It is showed that extending the integration time and lowering the noise bandwidth have benefits on the accuracy and loss-of-lock durations of the tracking measurements up to a point. Furthermore, although KF-based carrier tracking outperforms the PLL-based tracking, it can also fail under both strong amplitude and phase scintillation conditions, yet it performs with no loss-of-lock duration under phase scintillation events.

REFERENCES

[1] Official U.S. government information about the Global Positioning System (GPS) and related topics. [Online]. Available: https://www.gps.gov/systems/gps/modernization/civilsignals/, Accessed: Oct. 18, 2018.

[2] P. Enge
GPS modernization: Capabilities of the new civil signals
Presented at the 10th Australian International Aerospace Congress, Brisbane, Australia, 2003. [Online]. Available: http://web.stanford.edu/group/scpnt/gpslab/pubs/papers/Enge_AIAC_2003.pdf

[3] C. Cristodaro, F. Dovis, N. Linty, and R. Romero
Design of a configurable monitoring station for scintillations by means of a GNSS software radio receiver
IEEE Geosci. Remote Sens. Lett., vol. 15, no. 3, pp. 325–329, Mar. 2018.

[4] P. M. Kintner, T. E. Humphreys, and J. C. Hinks
GNSS and ionospheric scintillation – how to survive the next solar maximum
Inside GNSS, vol. 4, no. 4, pp. 22–3, Jul.–Aug. 2009. [Online]. Available: http://www.insidegnss.com

[5] D. Borio, C. O'Driscoll, and G. Lachapelle
Coherent, noncoherent, and differentially coherent combining techniques for acquisition of new composite GNSS signals
IEEE Trans. Aerosp. Electron. Syst., vol. 45, no. 3, pp. 1227–1240, Jul. 2009.

[6] F. Dovis and T. Hai Ta
High sensitivity techniques for GNSS signal acquisition
Global Navigation Satellite Systems, S. Jin, Ed., Rijeka, Croatia: IntechOpen Feb. 2012, ch. 1, pp. 3–32.

[7] C. Savas, F. Dovis, and G. Falco
Performance evaluation and comparison of GPS l5 acquisition methods under scintillations
In *Proc.31st Int. Tech. Meet. Satell. Division Inst. Navigation*, Sep. 2018, pp. 3596–3610.

[8] M. Petovello
Ionospheric scintillation
Inside GNSS, Jan. 19, 2014. [Online]. Available: https://insidegnss.com/ionospheric-scintillation/

[9] Z. Bo and G. Lachapelle
Acquisition schemes for a GPS l5 software receiver
In *Proc. 17th Int. Tech. Meet. Satell. Division Inst. Navigation*, Long Beach, CA, Sep. 2004, pp. 1035–1040.

[10] D. Borio, C. Mongredien, and G. Lachapelle
New L5/E5a acquisition algorithms: Analysis and comparison
In *Proc. 10th IEEE Int. Symp. Spread Spectr. Techn. Appl.*, Bologna, Italy, Aug. 2008, pp. 53–57.

[11] C. Hegarty, M. Tran, and A. J. Van Dierendonck
Acquisition algorithms for the GPS l5 signal
In *Proc. 16th Int. Tech. Meet. Satell. Division Inst. Navigation*, Portland, OR, USA, Sep. 2003, pp. 165–177.

[12] C. Yang, C. Hegarty, and M. Tran
Acquisition of the GPS l5 signal using coherent combining of I5 and Q5
In *Proc. 17th Int. Tech. Meet. Satell. Division. Inst. Navigation*, Long Beach, CA, USA, Sep. 2004, pp. 2184–2195.

[13] M. Susi, M. Aquino, R. Romero, F. Dovis, and M. Andreotti
Design of a robust receiver architecture for scintillation monitoring
In *Proc. IEEE/ION Position, Location Navigation Symp.*, Monterey, CA, USA, 5–8 May 2014, pp. 73–81

[14] L. Zhang, Y. T. Morton, and M. M. Miller
A variable gain adaptive Kalman filter-based GPS carrier tracking algorithm for ionosphere scintillation signals
In *Proc. 23rd Int. Tech. Meet.Satell. Division Inst. Navigation*, Portland, OR, USA, Sep. 2010, pp. 3107–3114.

[15] J.-H. Won, B. Eissfeller, T. Pany, and J. Winkel
Advanced signal processing scheme for GNSS receivers under ionospheric scintillation

In *Proc. IEEE/ION Position, Location Navigation Symp.*, Myrtle Beach, SC, USA, Apr. 2012, pp. 44–49

[16] T. E. Humphreys, M. L. Psiaki, and P. M. Kintner
GPS carrier tracking loop performance in the presence of ionospheric scintillations
In *Proc. 18th Int. Tech. Meet.Satell. Division*, Long Beach, CA, USA, Sep. 2005, pp. 156–167

[17] J. VilàValls, P. Closas, and C. Fermlndez-Prades
Advanced KF-based methods for GNSS carrier tracking and ionospheric scintillation mitigation
In *Proc. IEEE Aerosp. Conf.*, Big Sky, MT, USA, 2015, pp. 1–10.

[18] T. E. Humphreys, M. L. Psiaki, B. O'Hanlon, and P. M. Kintner
Simulating ionosphere-induced scintillation for testing GPS receiver phase tracking loops
IEEE J. Sel. Topics Signal Process., vol. 3, no. 4, pp. 707–715, Aug. 2009.

[19] V. Barreau, W. Vigneau, C. Macabiau, and L. Deambrogio
Kalman filter based robust GNSS signal tracking algorithm in presence of ionospheric scintillations
In *Proc. 6th ESA Workshop Satell. Navigation Technol. Eur. Workshop GNSS Signals Signal Process.*, Noordwijk, 2012, pp. 1–8, doi: 10.1109/NAVITEC.2012.6423045.

[20] A. Ferrario, A. Zin, L. Siniscalco, A. Emmanuele, N. Pastori, and P. Crosta
Improvement of a high-grade GNSS receiver robustness against ionospheric scintillations using a kalman filter tracking scheme
In *Proc. 28th Int. Tech. Meet. Satell. Division Inst. Navigation*, Tampa, Florida, Sep. 2015, pp. 3116–3126.

[21] J. Secan, R. Bussey, E. Fremouw, and S. Basu
High-latitude upgrade to the wideband ionospheric scintillation
Radio Sci., vol. 32, no. 4, pp. 1567–1574, Jul. 1997.

[22] R. Tiwari, S. Skone, S. Tiwari, and H. J. Strangeways
WBMOD assisted PLL GPS software receiver for mitigating scintillation affect in high latitude region
In *Proc. 30th URSI General Assem. Scientific Symp.*, Istanbul, Turkey, 2011, pp. 1–4.

[23] A. J. Van Dierendonck, J. Klobuchar, and Q. Hua
Ionospheric scintillation monitoring using commercial single frequency c/a code receivers
In *Proc. 6th Int. Tech. Meeting of Satell. Division Inst. Navigation*, Sep. 1993, pp. 1333–1342.

[24] N. Linty, F. Dovis, and L. Alfonsi
Software-defined radio technology for GNSS scintillation analysis: Bring antarctica to the lab
GPS Solutions, vol. 22, no. 4, Jul. 2018, Art. no. 96.

[25] L. Alfonsi *et al.*
First observations of GNSS ionospheric scintillations from demogrape project
Space Weather, vol. 14, no. 10, pp. 704–709, Sep. 2016.

[26] Y. Jiao, Y. Morton, and S. Taylor
Comparative studies of high-latitude and equatorial ionospheric scintillation characteristics of GPS signals
In *Proc. IEEE/ION Position, Location Navigation Symp.*, Monterey, California, May 5–8, 2014, pp. 37–42.

[27] K. S. Jacobsen and M. Dahnn
Statistics of ionospheric disturbances and their correlation with gnss positioning errors at high latitudes
J. Space Weather Space Climate, vol. 4, Sep. 2014, Art. no. A27.

[28] IS-GPS-705D Navstar GPS Space Segment/User Segment L5 Interfaces Document
Sep. 24, 2013. [Online]. Available: https://www.gps.gov/technical/icwg/IS-GPS-705D.pdf

[29] S. J. Hrbek, D. H. Won, and D. M. Akos
Power characterization for l1 and l5 transmissions
In *Proc. 19th Int. Tech. Meeting Inst. Navigation*, Monterey, California, Jan. 2016, pp. 873–880.

[30] C. Mongredien, G. Lachapelle, and M. E. Cannon
Testing GPS l5 acquisition and tracking algorithms using a hardware simulator
In *Proc. 19th Int. Tech. Meet. Satell. Division Inst. Navigation*, Fort Worth, TX, Sep. 2006, pp. 2901–2913.

[31] F. Bastide, O. Julien, C. Macabiau, and B. Roturier
Analysis of l5/e5 acquisition, tracking and data demodulation thresholds
In *Proc. 15th Int. Tech. Meet. Satell. Division Inst. Navigation*, Portland, OR, Sep. 2002, pp. 2196–2207.

[32] Y. Chun
FFT acquisition of periodic, aperiodic, puncture, and overlaid code sequences in GPS
In *Proc. 14th Int. Tech. Meet. Satell. Division Inst. Navigation*, Salt Lake City, UT, Sep. 2001, pp. 137–147.

[33] M. Pini, L. Lo Presti, and E. Viviani
GPS l5 signal acquisition exploiting Neumann-Hoffman code transitions
In *Proc. Int. Tech. Meet. Inst. Navigation*, San Diego, CA, Jan. 2010, pp. 765–772.

[34] G. E. Corazza, C. Palestini, R. Pedone, and M. Villanti
Galileo primary code acquisition based on multi-hypothesis secondary code ambiguity elimination
In *Proc. 20th Int. Tech. Meet. Satell. Division Inst. Navigation*, Fort Worth, TX, Sep. 2007, pp. 2459–2465.

[35] D. Borio
M-sequence and secondary code constraints for gnss signal acquisition
IEEE Trans. Aerosp. Electron. Syst., vol. 47, no. 2, pp. 928–945, Apr. 2011.

[36] N. C. Shivaramaiah, A. G. Dempster, and R. Chris
Exploiting the secondary codes to improve signal acquisition performance in Galileo receivers
In *Proc. 21st Int. Tech. Meet. Satell. Division Inst. Navigation*, Savannah, GA, Sep. 2008, pp. 1497–1506.

[37] J. Leclère, C. Botteron, and P.-A. Farine
High sensitivity acquisition of GNSS signals with secondary code on FPGAs
IEEE Aerosp. Electron. Syst. Mag., vol. 32, no. 8, pp. 46–63, Aug. 2017.

[38] J. Leclère and R. J. Landry
Combining secondary code correlations for fast GNSS signal acquisition
In *Proc. IEEE/ION Position, Location Navigation Symp.*, Apr. 2018, pp. 46–55.

[39] J. B. Y. Tsui
Fundamentals of Global Positioning System Receivers: A Software Approach, 2nd ed., New York, NY, USA: Wiley, Nov. 2004.

[40] D. Borio
A statistical theory for GNSS signal acquisition
Ph.D. dissertation, Dept. Electron. Telecommun., Politecnico di Torino, Turin, Italy, Mar. 2008.

[41] P. W. Ward, J. W. Betz, and C. J. Hegarty
Satellite signal acquisition, tracking and data demodulation
Understanding GPS: Principles and Applications, 2nd ed. Nordwood, MA: Artech House, 2006.

[42] J. VilàValls, P. Closas, M. Navarro, and C. Prades-Fernandez
Are PLLs dead? A tutorial on kalman filter-based techniques for digital synchronization
IEEE Aerosp. Electron. Syst. Mag., vol. 32, no. 7, pp. 28–45, Jul. 2017.

[43] R. Yang, K-V. Ling, E-K. Poh, and Y. Morton
Generalized GNSS signal carrier tracking: Part I—modeling and analysis

IEEE Trans. Aerosp. Electron. Syst., vol. 53, no. 4, pp. 1781–1796, Aug. 2017.

[44] J.-H. Won, D. Dotterbock, and B. Eissfeller
Performance comparison of different forms of Kalman filter approaches for a vector-based GNSS signal tracking loop
Navigation, J. Inst. Navigation, vol. 57, no. 3, pp. 185–199, Fall 2010.

[45] P. M. Kintner, B. M. Ledvina, and E. R. De Paula
GPS and ionospheric scintillations
Space Weather, vol. 5, no. 9, 2007, Art. no. S09003.

[46] A. J. Van Dierendonck
GPS receivers
in Global Positioning System: Theory and Applications,, vol. 1, B. W. Parkinson and J. J. Spilker Jr. Eds., Amer. Inst. Aeronaut. Astronaut., Washington DC, 1996, ch. 8.

[47] S. Stevanovic and B. Pervan
A GPS phase-locked loop performance metric based on the phase discriminator output
Sensors, vol. 18, no. 1, 2018, Art. no. 296

[48] C. Mongredien, M. E. Cannon, and G. Lachapelle
Performance evaluation of Kalman filter based tracking for the new GPS l5 signal
In *Proc. 20th Int. Tech. Meet. Satell. Division Inst. Navigation*, Fort Worth, TX, Sep. 2007, pp. 749–758.

[49] X. Tang, G. Falco, E. Falletti, and L. L. Presti
Theoretical analysis and tuning criteria of the Kalman filter-based tracking loop
GPS Solutions, vol. 19, pp. 489–503, 2015.

[50] N. Linty, A. Minetto, F. Dovis, and L. Spogli
Effects of phase scintillation on the GNSS positioning error during the september 2017 storm at Svalbard
Space Weather, vol. 16, no. 9, pp. 1317–1329, 2018.

[51] P. J. Cilliers *et al.*
Analysis of the ionospheric scintillations during 20–21 Jan. 2016 from SANAE by means of the DemoGRAPE scintillation receivers
In *Proc. 32nd General Assem. Scientific Symp. Int. Union Radio Sci.*, Jan. 2017, pp. 1–4.

Caner Savas received the M.Sc. degree in telecommunications from Middle East Technical University, Ankara, Turkey, in 2014. He is currently working toward the Ph.D. degree with the Department of Electronics and Telecommunications, Politecnico di Torino, Turin, Italy.

He is involved in software and hardware implementations of both navigation and radar systems with different companies. His research interest includes the implementation of a carrier-based software GNSS receiver.

Gianluca Falco received the M.Sc. and Ph.D. degrees in electronics and communication engineering from Politecnico di Torino, Turin, Italy in 2007 and 2011, respectively.

He is currently a Communication Engineer with the Space and Navigation Technologies research area of the LINKS Foundation, Turin, Italy. His research interest focuses on multisensors fusion, particularly between GPS and inertial navigation systems, as well as on advanced processing techniques for dual frequency and multiconstellation GNSS receivers.

Fabio Dovis received the M.Sc. and Ph.D. degrees in electronics and communications engineering from Politecnico di Torino, Turin, Italy, in 1996 and 2000, respectively.

He is currently an Associate Professor with the Department of Electronics and Telecommunications, Politecnico di Torino, Turin, Italy, where he coordinates the Navigation Signal Analysis and Simulation (NavSAS) group. His research interests include the design of GPS and Galileo receivers and advanced signal processing for interference and multipath detection and mitigation, as well as ionospheric monitoring.

Prof. Dovis is a member of the IEEE AESS navigation systems panel, and he has a relevant experience in international projects in cooperation with industries in the field of satellite navigation.